Lattice Boltzmann simulation of turbulence-induced flocculation of cohesive sediment

Jin-Feng Zhang · Qing-He Zhang · Jerome P.-Y. Maa · Guang-Quan Qiao

Abstract Both the floc formation and floc breakup of cohesive sediment are affected by turbulent shear which is recognized as one of the most important parameters, and thus, on the settling and transport of cohesive sediment. In this study, the development of floc characteristics at early stage and steady-state of flocculation were investigated via a three-dimensional lattice Boltzmann numerical model for turbulence-induced flocculation. Simulations for collision and aggregation of various size particles, floc growth, and breakup in isotropic and homogenous turbulent flows with different shear stresses were conducted. Model results for the temporal evolution of floc size distribution show that the normalized floc size distributions is time-independent during early stage of flocculation, and at steady-state, shear rate has no effect on the shape of normalized floc size distribution. Furthermore, the size, settling velocity, and effective density of flocs at the non-equilibrium flocculation stage do not change significantly for shear stresses in the range 0–0.4 N m^{-2}. The relationships between floc size and settling velocity established during floc growth stages and that during steady-states are different.

Responsible Editor: Andrew James Manning

J.-F. Zhang (✉) · Q.-H. Zhang · G.-Q. Qiao
State Key Laboratory of Hydraulic Engineering Simulation and Safety, Tianjin University, Tianjin 30072, China
e-mail: jfzhang@tju.edu.cn

J. P.-Y. Maa
Department of Physical Sciences, Virginia Institute of Marine Science, School of Marine Science, College of William and Mary, Gloucester Point, VA 23062, USA

1 Introduction

Flocculation of cohesive sediments is closely related to many phenomena, such as the estuarine turbidity maximum, channel siltation, and contaminant transport and deposition, etc. In estuaries and coastal areas, the flocculation is mainly driven by turbulent shear force (Winterwerp 1998). It is suggested that the particle collision, aggregation, and breakup frequency depends largely on the turbulence intensity (Manning 2004; Winterwerp et al. 2006).

To understand multi-particle aggregation under turbulent shear stress, most studies have been carried out based on theoretical analysis, laboratory experiments, and field observations (Amos and Droppo 1996; Spicer and Pratsinis 1996; Manning and Dyer 1999; Manning 2004; Manning et al. 2007; Maggi 2005; Maggi et al. 2007; Winterwerp et al. 2006; Mietta et al. 2009; Ha and Maa 2010; Frappier et al. 2010). Researches on numerical simulations of flocculation process in turbulent fluids are scarce. Previous works involving numerical model mainly contain two methods. The first one is determining the particle collision frequency function and estimating the sediment size distribution based on the Smoluchowski framework with some assumptions (McCave 1984; Winterwerp 1998; Lee et al. 2000; Xu et al. 2008; Maggi et al. 2007). Winterwerp (1998) proposed a Lagrangian population balance equation to describe the time evolution of the floc size distribution. Later, a modified method of changing the fractal dimension of flocs during flocculation within a population balance equation was proposed by Maggi et al. (2007). The second method is investigating floc formation and breakup in shear flow by considering the interactions between flocs and fluid through the use of a discrete

element method that simulate the deformation and breakup of large aggregates in two-dimensional or three-dimensional (3D) flows (Higashitani and Iimura 1999; Higashitani et al. 2001). Zeidan et al. (2007) further combined continuum and discrete model to improve the evolution of aggregation deformation and breakup in a linearly increase simple shear flow.

It is generally acknowledged that the floc size (and thus, settling velocity) will increase with shear rate at low shear rate, whereas the opposite trend is known at larger shear rates (Manning and Dyer 1999; Manning 2004; Winterwerp et al. 2006). However, many questions have not been resolved yet, e.g., how the flocculation is promoted at low shear stress? And how the flocs are disrupted at larger shear stress? Furthermore, how to simulate turbulence-induced flocculation process, and how to determine the collision frequency and efficiency of particles due to turbulence? These questions require dealing with an individual floc, or having a mesoscopic view in the model, and thus, need further research. Therefore, a numerical model to address the above questions is of clear interest.

Lattice Boltzmann (LB) method is a kind of hydrodynamic model based on mesoscopic kinetic equations, which has successfully been developed to include solid particles in suspensions. Ladd (1994) is the first one that introduced LB method to simulate particles suspended in fluids. Cate et al. (2004) presented fully resolved simulations to trace all particles suspended in an isotropic turbulent flow field through LB method. Zhang and Zhang (2007) described the settling behavior of fractal floc in still water. Later, Zhang and Zhang (2011) further used the LB method to explore the flocculation due to differential settling in calm water. The effect of turbulence, however, has not been addressed yet and that leads to this study.

As a simple case of turbulent flows, homogeneous and isotropic turbulence is widely used in the study of sediment transport and pollutant dispersion. Turbulence has a strongly nonlinear dissipative characteristic. In a decaying turbulent flow, kinetic energy is produced at large scales, and dissipated at the small scales. Therefore, some kind of energy (i.e., shear forcing, or pressure gradient force) input has to be added to the flow in order to keep the level of turbulence. Besides decaying isotropic turbulence, forced isotropic turbulence is frequently used to study statistically stationary turbulent flows, which prevails for flow with higher Reynolds number than the decaying isotropic turbulence (Lundgren 2003). A forced homogeneous isotropic turbulence field is used as the turbulent field to simulate the sediment flocculation.

The objectives of this paper are (1) to describe the flocculation processes under different shear rates and explore the turbulence-induced flocculation mechanism; (2) to indicate the development of floc characteristics at early stage and steady-state of flocculations; (3) to examine the interaction forces and collision frequency between particles during flocculation. This paper is organized as follows: Model description is discussed in Section 2. Specifically, Lattice Boltzmann equation, boundary conditions, and hydrodynamic forces are described in details. In Section 3, initial homogenous isotropic turbulent flows and the corresponding parameter setting are described. Results and discussions are presented in Section 4, and conclusions are drawn in Section 5.

2 Model description

2.1 Lattice Boltzmann equation

The basic idea of LB method is to use a particle distribution function, $f(\mathbf{x}, t)$, and a simplified set of particle velocities, $\mathbf{e}_i$, at a lattice node to represent the fluid and its motion at that node. Here the bold characters, e.g., $\mathbf{x}$ and $\mathbf{e}_i$ are vectors or tensors, and this style is used in this study. According to boundary conditions and applied forces, at any discrete time step, particles at a fluid node move to neighboring nodes with these specified velocities $\mathbf{e}_i$, and meanwhile, it accepts particles from neighborhood fluid nodes, and thus, change the properties of fluid and its motion at each node. The LB equation describes the time evolution of $f_i(\mathbf{x}, t)$, as:

$$f_i(\mathbf{x} + \mathbf{e}_i \Delta t, t + \Delta t) = f_i(\mathbf{x}, t) + \Omega_i[\mathbf{f}(\mathbf{x}, t)] \quad (1)$$

where $\mathbf{e}_i$ is the ith velocity vector, pointing from a node, located at $\mathbf{x}$, to adjacent nodes. The subscript, i, in 3D flows may be up to 19 for a D3Q19 topology (shown as Fig. 1), i.e., a three-dimensional cubic lattice with 19 velocity vectors $\mathbf{e}_i$ ($i = 0, 1, 2, \ldots, 18$), where $i = 0$ corresponds to the zero vector, i.e., $\mathbf{e}_0 = 0$. This means some particles will stay at their original location. The collision operator $\Omega_i(\mathbf{f})$, depends on all the f_i's at the node, denoted collectively by $\mathbf{f}(\mathbf{x},t)$. It can be constructed by linearization about the local equilibrium f^{eq} (Ladd 1994):

$$\Omega_i(\mathbf{f}) = \Omega_i(\mathbf{f}^{\mathrm{eq}}) + \sum_j \ell_{ij} f_j^{\mathrm{neq}} \quad (2)$$

where the non-equilibrium particle distribution function, f_j^{neq}, defined as, $f_j - f_j^{\mathrm{eq}}$, and $\Omega_i(\mathbf{f}^{\mathrm{eq}}) = 0$. ℓ_{ij} are the matrix elements of the linearized collision operator, which must satisfy the following eigen-equations (Ladd and Verberg 2001):

$$\sum_i \ell_{ij} = 0, \sum_i \mathbf{e}_i \ell_{ij} = 0, \sum_i \overline{\mathbf{e}_i \mathbf{e}_i} \ell_{ij} = \lambda \overline{\mathbf{e}_j \mathbf{e}_j}, \sum_i e_i^2 \ell_{ij} = \lambda_v e_j^2 \quad (3)$$

where $\overline{\mathbf{e}_i \mathbf{e}_i}$ is the traceless part of $\mathbf{e}_i \mathbf{e}_j$. The first two equations follow from conservation of mass and momentum, and the last two equations describe the isotropic relaxation of the stress
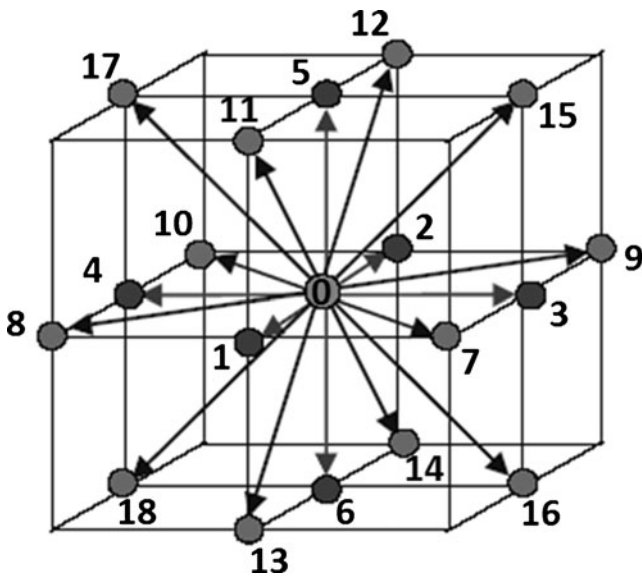
Fig. 1 Sketch of the 19 velocity vectors ($\mathbf{e}_i$, $i = 0, 1, \ldots, 18$) for the D3Q19 model

tensor; the eigenvalues λ and λ_v are related to the shear μ and bulk viscosities μ_v and lie in the range $-2 < \lambda < 0$, in which $\mu = -\rho c_s^2 \Delta t \left(\frac{1}{\lambda} + \frac{1}{2} \right)$ and $\mu_v = -\rho c_s^2 \Delta t \left(\frac{2}{3\lambda_v} + \frac{1}{3} \right)$. $c_s = \sqrt{c^2/3}$ is the speed of sound, where c is the particle speed, i.e. $c = \Delta x / \Delta t$, in which Δx is the lattice spacing.

The collision operator can be simplified by taking a single eigenvalue for both the viscous and kinetic modes. This exponential relaxation time approximation $\Omega_i = -f_i^{\text{neq}}/\tau$, i.e., lattice Bhatnagar–Gross–Krook method (Chen et al. 1992), has become the most popular form for the collision operator because of its simplicity and computational efficiency, where τ is the relaxation time. However, the absence of a clear time scale separation between the kinetic and dynamic modes of collision operator can sometimes cause significant errors at solid–fluid boundaries. For this reason, Ladd and Verberg (2001) suggested a 3-parameter collision operator, and that was used in this study.

Determining a suitable equilibrium distribution function plays an essential role in LB method. In particular, it will meet the mass, momentum, and momentum flux:

$$\rho(\mathbf{x}, t) = \sum_i f_i^{\text{eq}}(\mathbf{x}, t) \tag{4a}$$

$$\mathbf{j}(\mathbf{x}, t) = \rho(\mathbf{x}, t) \mathbf{u}(\mathbf{x}, t) = \sum_i f_i^{\text{eq}}(\mathbf{x}, t) \mathbf{e}_i \tag{4b}$$

$$\Pi(\mathbf{x}, t) = \sum_i f_i^{\text{eq}}(\mathbf{x}, t) \mathbf{e}_i \mathbf{e}_i \tag{4c}$$

where ρ is the mass density, $\mathbf{j}$ is the momentum density, and Π is the momentum flux.

The equilibrium distribution function f_i^{eq} of the D3Q19 model that satisfies Eq. 3, can be defined as (Ladd and Verberg 2001):

$$f_i^{\text{eq}} = w_i \rho \left[1 + \frac{\mathbf{e}_i \cdot \mathbf{u}}{c_s^2} + \frac{(\mathbf{e}_i \cdot \mathbf{u})^2}{2c_s^4} - \frac{(\mathbf{u} \cdot \mathbf{u})}{2c_s^2} \right] \tag{5}$$

where the weighting factors w_i equal to 1/3 ($i = 0$) for the rest particle, 1/18 ($i = 1, 2, \ldots, 6$) for the 6 coordinate directions and 1/36 ($i = 7, 8, \ldots, 18$) for the 12 bi-diagonal directions, respectively (Fig. 1).

The D3Q19 model has the following set of discrete velocities:

$$\mathbf{e}_i = \begin{cases} (0,0,0) & i = 0 \\ (0, \pm 1, 0)c, (\pm 1, 0, 0,)c, (0, 0, \pm 1)c & i = 1, 2, \ldots, 6 \\ (\pm 1, \pm 1, 0)c, (0, \pm 1, \pm 1)c, (\pm 1, 0, \pm 1)c & i = 7, 8, \ldots, 18 \end{cases} \tag{6}$$

The post-collision distribution $f_i^* = f_i + \Omega_i$ is written as a series of moments:

$$f_i^* = w_i \rho \left[1 + \frac{\mathbf{e}_i \cdot \mathbf{u}}{c_s^2} + \frac{(\mathbf{e}_i \cdot \mathbf{u})^2 + (\mathbf{e}_i \cdot \mathbf{e}_i \cdot \Pi^{\text{neq},*})}{2c_s^4} - \frac{(\mathbf{u} \cdot \mathbf{u} + \Pi^{\text{neq},*})}{2c_s^2} \right] \tag{7}$$

The non-equilibrium second moment Π^{neq} is modified by the collision process:

$$\Pi^{\text{neq},*} = (1 + \lambda) \overline{\Pi^{\text{neq}}} + \frac{1}{3}(1 + \lambda_v)\Pi^{\text{neq}} + \frac{1}{3}(1 + \lambda_v) \tag{8}$$

where $\Pi^{\text{neq}} = -\Pi^{\text{eq}}$, $\Pi^{\text{eq}} = \sum_i \mathbf{e}_i \mathbf{e}_i f_i^{\text{eq}} = \rho c_s^2 + \rho \mathbf{u} \cdot \mathbf{u}$.

In the presence of an externally imposed force density $\mathbf{F}$, for example, a pressure gradient, a gravitational field or interaction forces between particles, the time evolution of the LB model includes an additional contribution in i direction, $F_i(\mathbf{x}, t)$:

$$f_i(\mathbf{x} + e_i \Delta t, t + \Delta t) = f_i^*(\mathbf{x}, t) + F_i(\mathbf{x}, t) \tag{9}$$

This forcing term can also be expanded in a power series in the velocity:

$$F_i = w_i \left[\frac{\mathbf{f} \cdot \mathbf{e}_i}{c_s^2} + \frac{(\mathbf{u} \cdot \mathbf{f} + \mathbf{f} \cdot \mathbf{u})(\mathbf{e}_i \cdot \mathbf{e}_i - c_s^2)}{2c_s^4} \right] \Delta t \tag{10}$$

The incompressible Navier–Stokes equations can be derived from the lattice Boltzmann equation using the Chapman–Enskog expansion (Chen et al. 1992).

2.2 Solid–fluid boundary condition

The LB method is well-suited for the problem of modeling solid particle suspensions because of its ability to solve particles movement with arbitrary shapes and complex geometries (Chen and Doolen 1998). The boundary conditions at the solid–fluid interface can be correctly and easily imposed. For a stationary interface, a no-slip boundary condition is easily implemented by using the bounce-back method. For a moving interface, the modified bounce-back method, where the boundary is always assumed to be located at the middle of the boundary links (shown as Fig. 2), has been introduced to match the velocity of the solid surface at the boundary node and to account for the momentum transfer to the solid particle (Ladd 1994). To account for the momentum change, Nguyen and Ladd (2002) proposed adding a term to the distribution function:

$$f_{i'}(\mathbf{x}, t + \Delta t) = f_i(\mathbf{x}, t_+) - 2B_i(\mathbf{u}_b \cdot \mathbf{e}_i) \tag{11}$$

where B is a coefficient proportional to the mass density of the fluid and depends on the detailed lattice structure. $\mathbf{x}$ is the position of the node adjacent to the solid-boundary with velocity $\mathbf{u}_b$, t_+ is the time immediately after the collision, i' is the reflected direction, which is the opposite of the incident direction i. $\mathbf{u}_b$ is determined by the solid-particle translational velocity $\mathbf{U}$, angular velocity Ω_b, and the position vector of the center of the solid particle $\mathbf{X}$:

$$\mathbf{u}_b = \mathbf{U} + \Omega_b \times (\mathbf{x}_b - \mathbf{X}) \tag{12}$$

where $\mathbf{x}_b = \mathbf{x} + \frac{1}{2}\mathbf{e}_i\Delta t$ is the location of the boundary node.

Thus, the momentum is exchanged locally between the fluid and the solid particle. To conserve the combined momentum of solid and fluid, the forces exerted at the boundary nodes can be calculated from the momentum transferred in Eq. (13):

$$\mathbf{F}_b\left(\mathbf{x} + \frac{1}{2}\mathbf{e}_i\Delta t, t + \frac{1}{2}\Delta t\right) = \mathbf{e}_i[2f_i(\mathbf{x}, t_+) - 2B_i(\mathbf{u}_b \cdot \mathbf{e}_i)] \tag{13}$$

2.3 Aggregate formation

Consider a three-dimensional large aggregate of arbitrary shape composed of N spherical solid particles of radius a_i and mass density ρ. The translational and rotational motions of a particle i in an aggregate are expressed by the following equations:

$$m\frac{d\mathbf{U}_{pi}}{dt} = \mathbf{F}_i \tag{14a}$$

$$I\frac{d\omega_{pi}}{dt} = \mathbf{M}_i \tag{14b}$$

where m and I are the mass and moment of inertia of a particle, respectively, $\mathbf{U}$, ω, $\mathbf{F}$ and $\mathbf{M}$ are the velocity, angular velocity, the total force, and total torque acting on the particle, respectively, and the suffix i indicates the constitutive particle i. Since the particle motion is determined by both the contributions of the hydrodynamic drag and the interaction with neighboring particles, excluding gravitational and buoyancy force, the following should be used as the force and torque on sediment particles, respectively (Higashitani et al. 2001):

$$\mathbf{F}_i = \mathbf{F}_{di} + \sum_j \mathbf{F}_{mij} \tag{15a}$$

$$\mathbf{M}_i = \mathbf{M}_{di} + a_i\sum_j \mathbf{F}_{mij} \times \mathbf{n}_{ij} \tag{15b}$$

where $\mathbf{F}_{di}$ and $\mathbf{M}_{di}$ are the hydrodynamic drag force and torque, respectively, $\mathbf{F}_{mij}$ is the mutual interaction force imposed on the particle i by the particle j, and $\mathbf{n}_{ij}$ is the unit vector defined by the following equation:

$$\mathbf{n}_{ij} = \mathbf{x}_{ij}/x_{ij} \tag{16}$$

where $\mathbf{x}_{ij} = \mathbf{x}_i - \mathbf{x}_j$, $x_{ij} = |\mathbf{x}_{ij}|$ and $\mathbf{x}_i$ is the position vector of the center of particle i.

The hydrodynamic drag force on the solid particle is calculated by summing impulses exerted on the particle by fluid particles (Hill et al. 2001). The hydrodynamic drag force acts on the outside particles is transmit to the inside particles through the interactions between them. Two kinds of mechanisms are considered. When particles are not contacting, particles interact with each other through the interaction forces given by the Derjaguin–Landau–Verwey–Overbeek theory (Verway and Overbeek 1948; Higashitani et al. 2001), such as the van der Waals attractive force $\mathbf{F}_{aggr,ij}$ and electrostatic repulsive force $\mathbf{F}_{repu,ij}$. In this study, only spherical primary particles are considered with the assumption that they all have the same electronic charges, uniformly distributed on their surface, and thus, there is no concern on the face-to-face flocculation nor the face-to-edge flocculation. Only the electronic repulsive force is considered. When two spheres approach each other, the fluid between these two spheres has to move away in order to allow these two particles to contact, this causes some resistance. Nguyen and Ladd (2002) named this as lubrication force $\mathbf{F}_{cont,ij}$. Full details about the lubrication force can be found in Kim and Karrila (1991).

After Russel et al. (1989), the van der Waals force between spherical particles i and j is:

$$\mathbf{F}_{aggr,ij} = \frac{A}{6}\left(-\frac{(a_i + a_j)^2 x_{ij}}{x_{ij}^2 - (a_i + a_j)^2} - \frac{(a_i + a_j)^2}{x_{ij}^3} + \frac{2x_{ij}}{x_{ij}^2 - (a_i + a_j)^2} - \frac{2}{x_{ij}}\right) \tag{17}$$
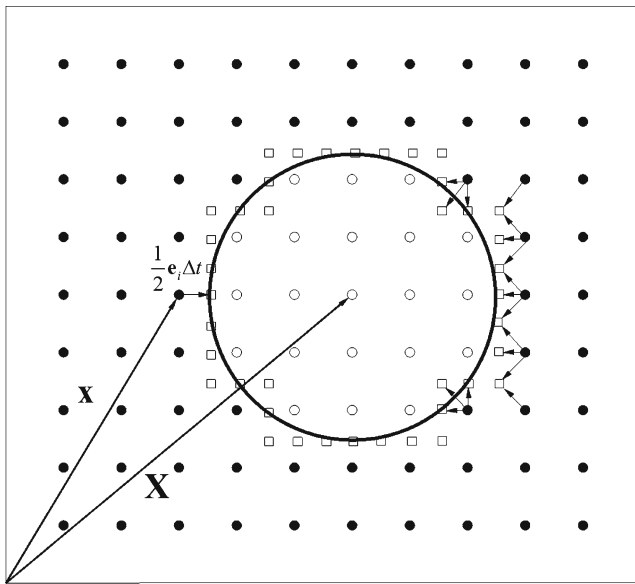
Fig. 2 Diagram of the lattice nodes with a moving particle (*the large circle with heavy solid line*). The moving particle boundary is represented by the *hollow squares*. The velocities along links cutting the boundary surface are indicated by *arrows*. The hollow circle at **X** represents the center of the moving particle, **x** is the position of the node adjacent to the solid-boundary and e_i is the ith velocity vector

where a_i and a_j are radii of two particles, $A \approx 10^{-20}$ J, is the Hamaker constant, which depends on the geometry and materials of the solid surface (Hamaker 1937).

According to Stern's theory of double layer (Hiemenz 1986), the electrostatic repulsive force between two particles with diameters a_i and a_j can be written as:

$$\mathbf{F}_{repu,ij} = \frac{4\pi\varepsilon_a \kappa a_i a_j \varphi^2}{a_i + a_j}\exp\left(-\kappa x_{ij}\right) \qquad (18)$$

where $\varepsilon_a = \varepsilon_0\varepsilon_r$ is the absolute dielectric constant of medium, ε_0 is the permittivity of vacuum ($\varepsilon_0 = 8.854 \times 10^{-12}$ F/m), ε_r is the dielectric constant of medium, which is 78.5 for water at 25 °C; κ is the reciprocal Debye length; φ is the surface electric potential of particles:

$$\varphi = \frac{2k_B T}{Z\chi}\ln\frac{1 + \exp(-\kappa t_h)}{1 - \exp(-\kappa t_h)}\mathrm{sign}(\varphi_0) \qquad (19)$$

where k_B is the Boltzmann constant, T is the absolute temperature, Z is the valence of the positive ion in the solution, χ is the electron charge; φ_0 is the reference potential, $\mathrm{sign}(\varphi_0) = 1$ when $\varphi_0 > 0$, $\mathrm{sign}(\varphi_0) = -1$ when $\varphi_0 < 0$; t_h is the hydrate water

thickness when φ equals to zeta potential, and t_h becomes infinity when if φ is not equal to zeta potential. The effect of water salinity on flocculation processes (Liu et al. 2007) was reflected by the electrostatic repulsive force (Eqs. 18 and 19). When the salinity is $s = 5$ ppt, these coefficients in Eq. (19) are listed in Table 1.

Based on acting forces, sediment particles will move in the water. When the gap between particles is less than 1.0 % of the primary diameter, Zhang and Zhang (2011) considered a successful aggregation. They introduced this idea of minimum separation gap into the LB modeling for simulating differential settling. Aggregates are composed of randomly packed spherical particles, and all primary particles in this group will move together as one aggregate. Pore water inside it also follows with the aggregate movement (Zhang and Zhang 2009).

2.4 Aggregate breakup

The rate of breakup of flocs and the equilibrium size of flocs in turbulent flow depend on their strength, F_c. Winterwerp (1998) suggested:

$$F_c = \frac{\pi}{4}d_f^2\tau_B \qquad (20)$$

where d_f is the floc size and τ_B is the yield stress, which is defined as (Tang et al. 2001):

$$\tau_B = 1.1\frac{(d_f/d_0)^{D_F-3}}{1 - (d_f/d_0)^{D_F-3}}\left(\frac{F}{d_0^2}\right) \qquad (21)$$

where d_0 is the primary particle diameter, d_f is the floc size, D_F is the fractal dimension of the floc and F is the binding forces between particles, including the van der Waals attractive force, $\mathbf{F}_{aggr,ij}$, electrostatic repulsive force, $\mathbf{F}_{repu,ij}$ and lubrication force, $\mathbf{F}_{cont,ij}$. When the external force, $\mathbf{F}_e$, such as the shear force of the fluid imposed on the floc is larger than the floc strength F_c, it will break up.

3 Model implementation

A selected amount of sediment particles with different sizes from 3 to 5 μm are placed in the turbulent flow randomly. The information of turbulent flow field and sediment distribution

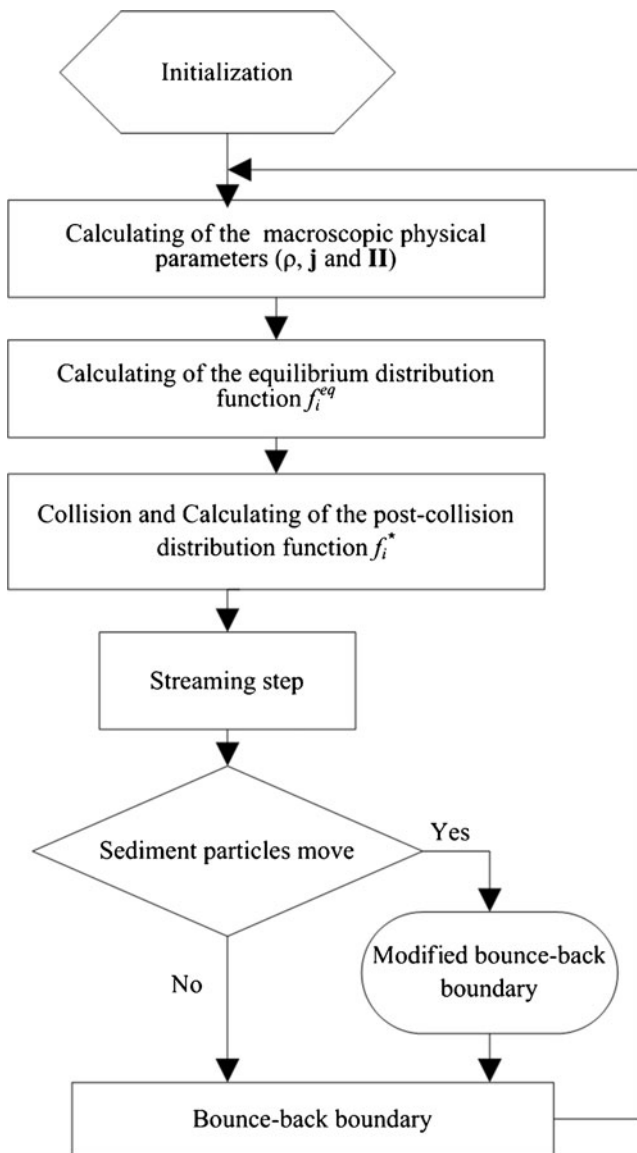| **Table 1** Coefficients in Eq. (19) based on the salinity of 5 ppt	k_B	T	e	κ^{-1}	t_h	φ
	1.38×10^{-23} J/K	298 K	1.6×10^{-19} C	0.98 nm	1.59 nm	19.9 mV

Fig. 3 Simulation procedure

is read into the numerical model as input conditions. Then settling and flocculation processes are computed in the LB

model by considering the interaction forces between particles and turbulent shears (Fig. 3).

3.1 Initial conditions

Initial homogeneous and isotropic turbulence flows were generated using pseudo-spectral method. In the model, the spectral forcing scheme is used to generate forced isotropic turbulence (Machiels 1997):

$$\widetilde{\mathbf{f}}(\mathbf{k},t) = \begin{cases} \varepsilon\widetilde{\mathbf{u}}(\mathbf{k},t)/[2E_f(t)], & 0<k<k_f \\ 0, & \text{others} \end{cases} \quad (22)$$

where ε is the energy dissipation rate; $\widetilde{\mathbf{u}}(\mathbf{k},t)$ is the velocity in Fourier space; k_f is the largest wave number; $E_f(t) = \int_0^{k_f} E(k,t)dk$, $E(k,t)$ is the energy spectra at the given time. From Eq. 22, we can see that there is no preferred direction and the turbulence will be homogenous and isotropic (Machiels 1997).

In the forced homogenous turbulence, an initial energy spectrum is given in Fourier space $\mathbf{k}$. In the present work, the following initial spectrum is used (Yan et al. 2010):

$$E_0(k) = Bk^4\exp(-0.14k^2), \quad k\in[k_a,k_b] \quad (23)$$

where the magnitude B and the range of the initial energy spectrum $[k_a, k_b]$ determine the initial total kinetic energy in the simulation. We use $B=1.4\times10^{-4}$, $k_a=3$ and $k_b=8$. The Taylor micro-scale Reynolds number is expressed as:

$$\text{Re}_\lambda = \frac{\lambda_T u_{\text{rms}}}{\nu} \quad (24)$$

where λ_T is the Taylor micro-scale length; u_{rms} is the root-mean-squared velocity; ν is the kinematic viscosity. In the model, the Taylor micro-scale Reynolds number is $17<\text{Re}_\lambda<156$. The probability density function of turbulent velocity

Fig. 4 Vorticity in the domain at different shear rates and its magnitude is larger than 0.005. a $G=8.8$ s^{-1}; b $G=12.8$ s^{-1}; c $G=17.6$ s^{-1}
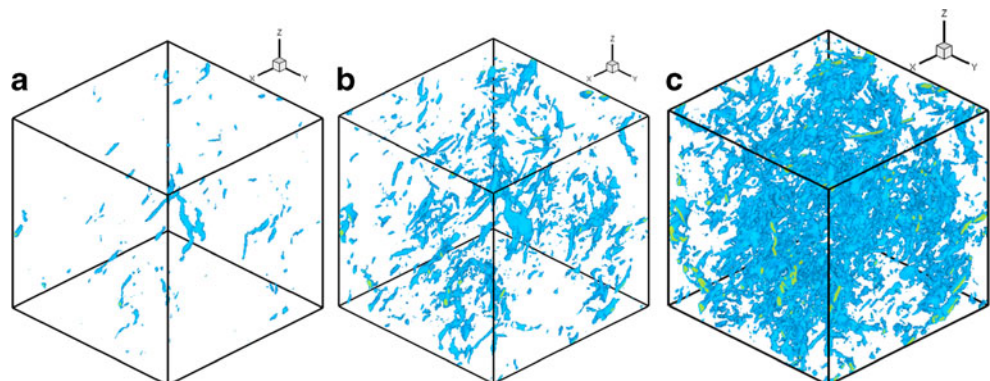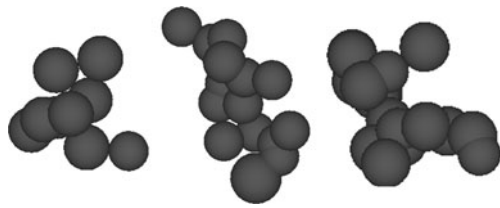
Fig. 5 Flocs generated by shear rate of 17.6 s^{-1} at initial sediment concentration of 2.0 kg m^{-3} during the early-stage flocculation ($t=10$ s)

fluctuations for x-, y- and z-directions appears a normal distribution with a mean of zero, respectively. The generated turbulence can be identified as isotropic.

By changing the value for ε, one will change the shear rate, G, in the turbulent flow because $G=(\varepsilon/\nu)^{1/2}$ (Camp and Stein 1943). In this study, eight shear rates ($G=3.1$, 4.7, 6.4, 8.8, 12.8, 17.6, 22.0, and 29.3 s^{-1}) are selected. The reasonable uniform spatial distribution of the vortical structures (for vorticity magnitude larger than 0.005) at three different shear rates (Fig. 4) can be a proof that it is an isotropic turbulent flow.

The turbulence shear stress (τ) is proportional to the turbulence kinetic energy E, assuming the energy production equals the energy dissipation and was calculated as $\tau=0.19 E$ (Manning 2004). Thus, the corresponding shear stresses, τ's, are 0.005, 0.01, 0.02, 0.04, 0.08, 0.2, 0.3, 0.4 N m^{-2}, respectively.

3.2 Parameter settings

Particles with diameters d_p of 3–5 μm distribute randomly in a fluid cell, and their densities are $\rho_s=2650$ kg m^{-3}. The following parameters are selected: fluid density, $\rho_w=1000$ kg m^{-3}, fluid kinematic viscosity, $\nu=1.0\times10^{-6}$ m^2 s^{-1}, gravity acceleration, $g=9.8$ m s^{-2}, the computation domain is 2.5 mm×2.5 mm× 2.5 mm, the volume concentration of particles is 7.55×10^{-4}, the
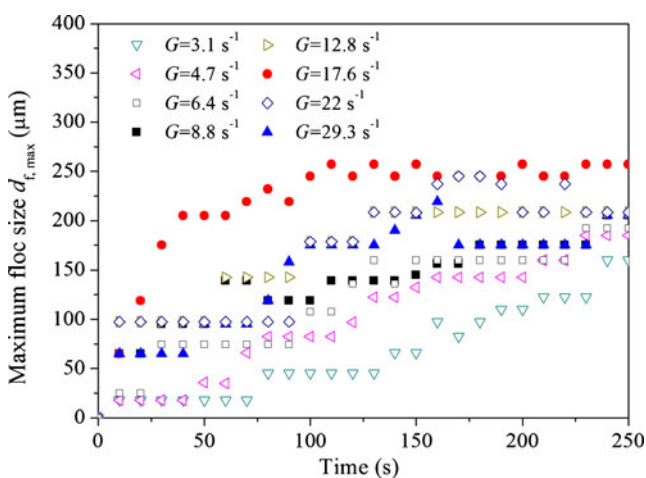

Fig. 6 Time evolution of maximum floc size in the domain for the different shear rates of 3.1, 4.7, 6.4, 8.8, 12.8, 17.6, 22.0, 29.3 s^{-1}
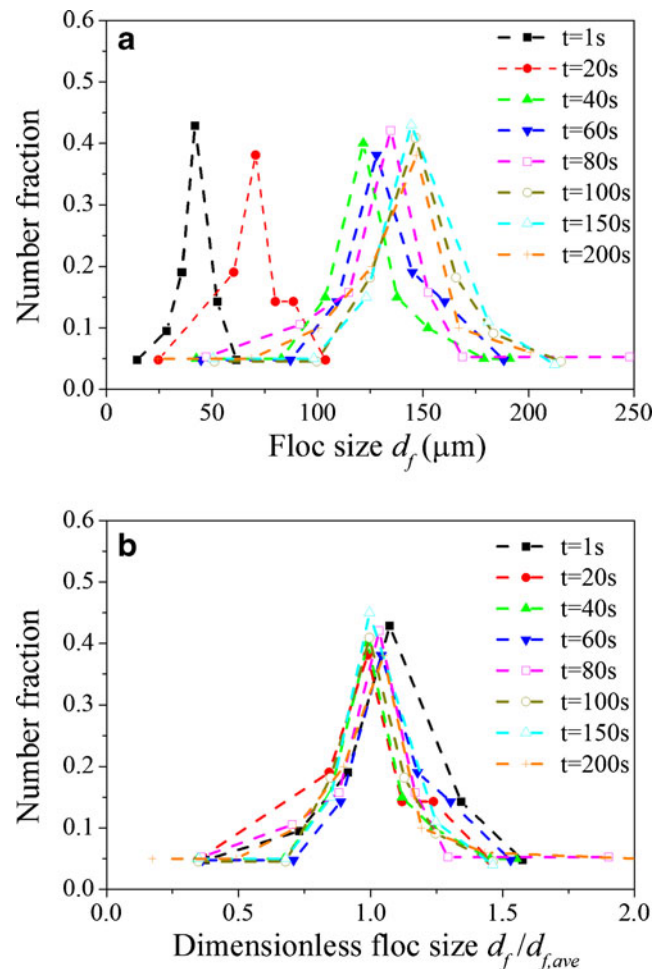

Fig. 7 Floc size distribution and normalized floc size distributions during floc growth for the shear rate $G=17.6$ s^{-1}

corresponding weight suspended sediment concentration is $c_m= 2.0$ kg m^{-3}, water salinity is 5 ppt, the grid number, $N=1280$, (N is defined as grid number in one direction) and the model is running with a time step interval of 6.67×10^{-7} s.

4 Numerical results and discussions

LB method has been successfully applied to simulate the settling process of fractal floc (Zhang and Zhang 2007) and flocculation processes of cohesive sediment due to differential settling (Zhang and Zhang 2011). Zhang and Zhang (2007, 2011) demonstrate that LB method is accurate and efficient after the numerical model is tested against laboratory experiments. In this section, the main results of the performed direct numerical simulations for turbulence-induced flocculation process are discussed. Floc properties, such as floc size, floc fractal dimension, floc density, and settling velocity, are analyzed. Subsequently, the interaction forces and collision efficiency between particles during flocculation are investigated.
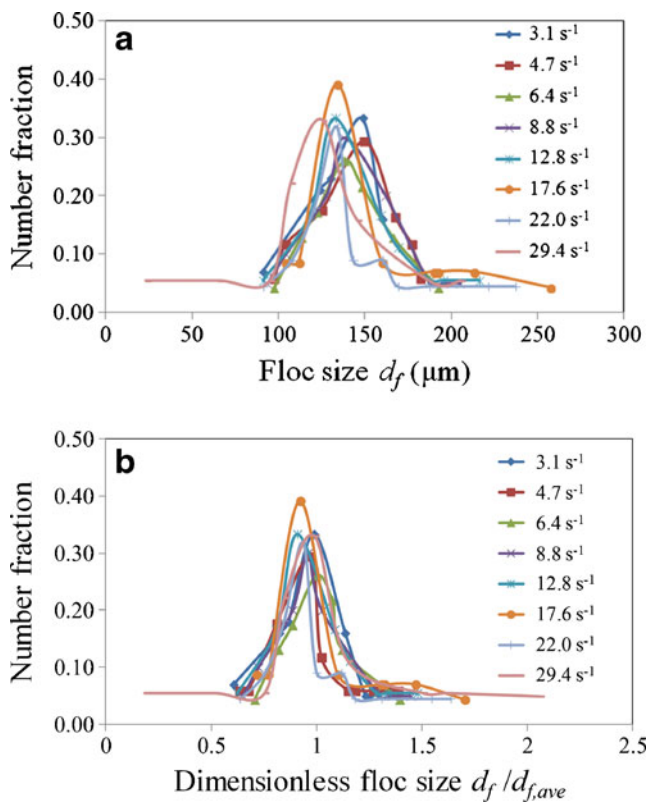
Fig. 8 **a** Steady-state floc size distributions as a function of shear rate at solid volume fraction $\varphi = 7.55 \times 10^{-4}$. **b** Normalized floc size distributions during steady-state for different shear rates

4.1 Time evolution of floc size

The fractal characterization of a floc can be calculated based on the concept of capacity dimension D_B, which is proposed by Liebovitch and Toth (1989) as:

$$D_B = \lim_{l \to 0} \frac{\log N_B(l)}{\log(1/l)} \tag{25}$$

This is called "box-counting" because one counts the minimal number of boxes $N_B(l)$, which cover the set of boxes of size l (l-covering). Figure 5 shows three flocs formed by a shear rate of 17.6 s⁻¹ at the time of 10 s, the particle number N_p in these three flocs are 9, 15, and 16, which have 3D capacity dimension D_B of 1.84, 1.89, and 2.03. The above three D_Bs agree well with that given by Huang (1994), 1.53–2.10, based on laboratory experiments.

The number of primary particles, N_p, within a floc can be obtained from D_B (Maggi et al. 2007):

$$N_p = \left(\frac{d_f}{d_p} \right)^{D_B} \tag{26}$$

where d_p is the average primary particle size and d_f is the floc size. When the number of primary particles N_p, is counted based

on the numerical result and the fractal dimension D_B is calculated, then the floc size d_f can be obtained by using Eq. (26).

The time history of maximum floc size in the domain for all the different shear rates suggested that the growth rate depends on the shear rate (Fig. 6). For aggregates formed by 3–5 μm primary particles at solid volume fraction $\varphi = 7.55 \times 10^{-4}$, the maximum aggregate size increases quickly at $G = 17.6$ s⁻¹ and reaches a stable status after about 100 s. For small shear rates, e.g., $G \leq 6.4$ s⁻¹, the increasing trend is small and continuous after 250 s, but for other shear rates, it reaches a stable size at the time of 180 s, which is close to that given by Frappier et al. (2010). Their study suggested that the average aggregate size reached a steady-state after about 200 s at $G = 3.7 \sim 82.5$ s⁻¹, for suspensions coagulated from 2 μm primary particles at the volume concentration of $\varphi = 10^{-3}$. The results in Fig. 6 also

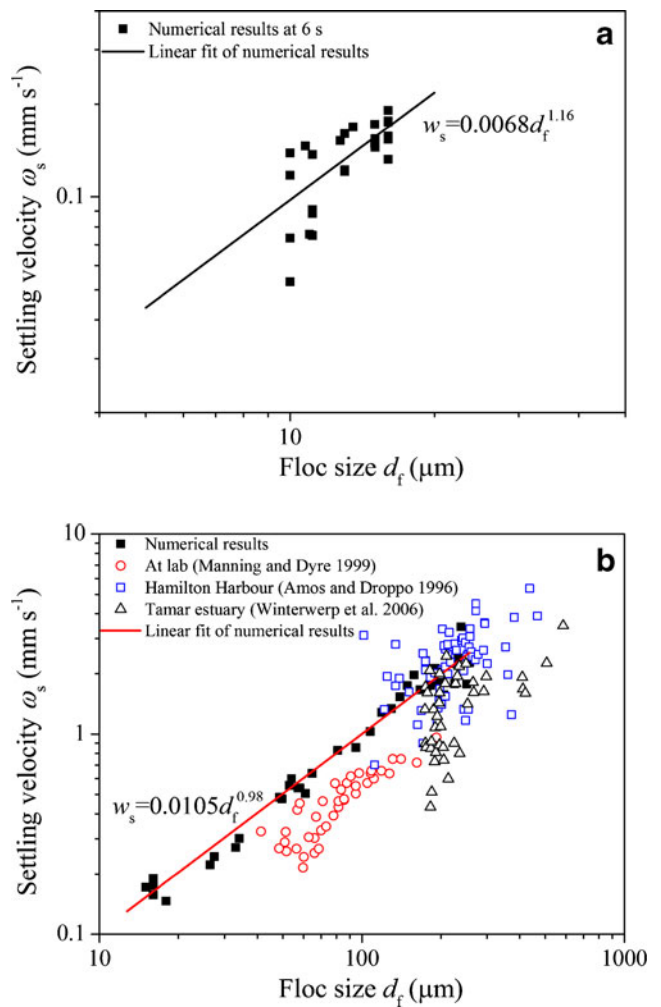**Fig. 9** Variations in settling velocity with floc size (**a**) at $t = 6$ s and (**b**) at $t = 200$ s. The *solid square* is the numerical results; the *hollow circle* expresses the experimental data (Manning and Dyer 1999); *hollow square* and *triangle* stand for the observations of floc settling velocities and floc size in the Hamilton Harbour (Amos and Droppo 1996) and in the Tamar estuary (Winterwerp et al. 2006), respectively. The *solid line* stands for linear fit of numerical results

Fig. 10 Variations in floc settling velocity and effective density over the turbulent shear range at sediment concentration of 2.0 kg m^{-3} and $t = 6$ s
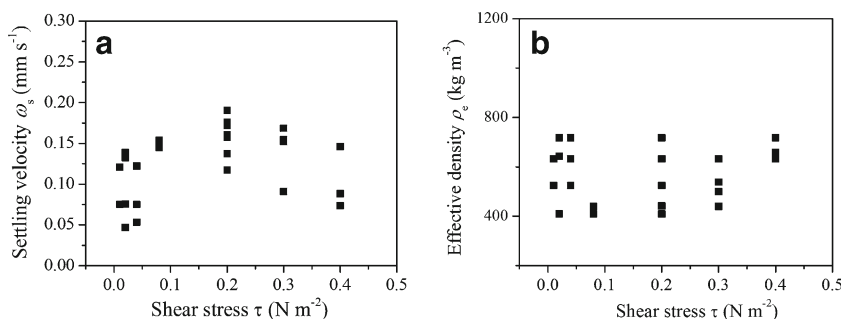
show that the turbulent shear rate has an impact on the maximum aggregate size: it tends to increase with G at low shear rates (e.g., $G < 17.6$ s^{-1}), but decrease as the shear rate further increases. This is because large G (e.g., $G = 29.3$ s^{-1}) will destruct flocs, especially large flocs.

4.2 Floc size distributions

During early-stage flocculation, floc size distribution varies with flocculation time. After about 100 s, the floc size distribution reaches a steady-state (Fig. 7a). Nevertheless, the dimensionless floc size $d_f/d_{f,ave}$ at any selected time, calculated from the simulation results, where $d_{f,ave}$ is the mean floc size at that time, shows (Fig. 7b) the normalized floc size distributions do not change with time, which is consistent with previous experimental results given by Frappier et al. (2010).

After reaching the steady-state of flocculation, the effects of shear rate on the steady-state floc size distribution (Fig. 8a) shows that high shear rates reduce the large tail of distribution and decrease the range of floc size distributions. Narrower distributions with an increase in shear rate were also reported by Spicer and Pratsinis (1996), for aluminum particles with a weight concentration of 32 mg/l, i.e., $\varphi = 8.3 \times 10^{-5}$. However, the normalized floc size distributions, when put together, are all close to each other and may be described by a single equation (Fig. 8b). This implies the shear rate has no effect on the shape of normalized steady-state floc size distribution, or independent with respect to shear rate. Hunt (1982) theoretically predicted self-similar size distributions during coagulation and verified experimentally with clay particles. This

phenomenon was also found from the flocculation of particles in a stirred tank at the laboratory (Spicer and Pratsinis 1996).

4.3 Floc settling velocity

The settling velocity of a sediment particle in the model is the vertical component of solid-particle translational velocity **U** (as shown in Eq. (12)), which is updated according to the forces applied on the particle. The velocities of particles increase significantly due to collision and adhesion between particles and then keep the floc settling velocity. So, the settling velocity of floc is obtained as mean settling velocities of particles that coagulate to form the floc. It was found that the mean settling velocity was basically the same as the entire floc settling velocity (Zhang and Zhang 2009).

During early-stage flocculation (i.e., 6 s after the simulation), the relation of floc size and settling velocity (Fig. 9a) indicates a power–law relationship. At this non-equilibrium stage, this relationship can be expressed as:

$$w_s = 0.0068 d_f^{1.16} \tag{27}$$

where w_s is in millimeter per second and d_f is in micrometer.

Floc effective density ρ_e is determined from the porosity p, where the porosity can be written in terms of capacity dimension D_B, $p = 1 - (d_f/d_p)^{D_B - 3}$, so the floc effective density can be expressed as:

Fig. 11 Temporal variation of x component force between two particles (#36 and 86) and the distance between these two particles during the first 8 s simulation when they are placed in an isotropic and homogenous turbulent flow with shear rate of 6.4 s^{-1} (or shear stress 0.02 N/m^{-2})
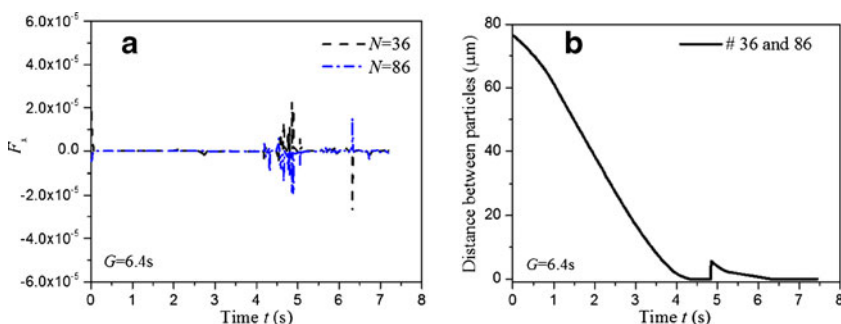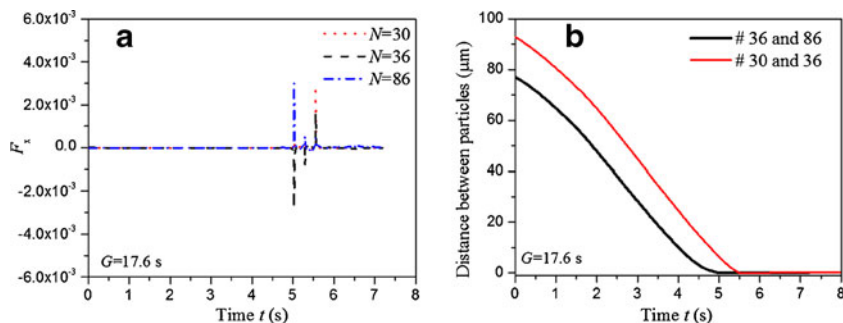
$$\rho_e = (\rho_s - \rho_w)(1-p) = (\rho_s - \rho_w)\left(\frac{d_p}{d_f}\right)^{3-D_B} \qquad (28)$$

From Fig. 10, we can see that the range of floc settling velocity is 0.05-0.2 mm s^{-1} and the excess density is in the range of 400–800 kg m^{-3}. As illustrated in Fig. 10, the floc settling velocity and excess density are substantially invariant with the shear stress, mainly because the flocculation was under non-equilibrium environmental conditions. For small time scales, the size, settling velocity and excess density of flocs do not change for shear stresses in the experimental range 0–0.4 N m^{-2}. When approaching steady-state (i.e., after about 200 s simulation), the relationship between floc size and settling velocity (Fig. 9b and Eq. 29) obtained from this numerical experiment shows a generally higher values than those obtained from lab and field experiments. This is mainly because the lab and field data don't have the perfect spherical primary particles as the building block. Other reasons, e.g., measurements at lab were made 120 s after the turbulence has ceased (Manning and Dyer 1999), unlike that turbulence is always existed in this numerical study.

With the assumption that the settling of individual flocs satisfies Stokes' law, at the equilibrium flocculation condition, the same empirical equation as Eq. (27) can be obtained:

$$w_s = 0.0105 d_f^{0.98} \qquad (29)$$

Comparison of the relation between floc size and settling velocity (Eq. 27) established during floc growth with the corresponding steady-state relation (Eq. 29), the settling velocity

$w_s \propto d_f^{1.16}$ under the non-equilibrium flocculation condition, a fractal dimension $D_B=2.16$ is found according to the simple relationship of the form $w_s \propto d_f^{D_B-1}$ (Winterwerp 1998); at the same time, a fractal dimension $D_B=1.98$ is obtained under the equilibrium flocculation condition, which is less than that during floc growth. D_B decreases slightly because of the forming of flocs with a looser structure at the steady-state.

4.4 Interaction forces

This LB simulation may reveal the inter-particle forces between particles. The following three examples are all with initial sediment concentration of 2.0 kg m^{-3}, and the sediment particle is numbered from 1 to N, such as particle 36 and 86 (Fig. 11).

When particles are sufficiently apart, the only force that acted on these particles would be drag force caused by flow turbulence (Fig. 11). The hydrodynamic drag force is relatively stable and only changes a little because of the isotropic and homogenous turbulence. As particle 36 and 86 are close to each other, other attractive forces become dominant. These two particles collide at time of about 4.5 s when the distance reduces to $0.01d_p$ and forces on the particle 36 and 86 increases sharply. Then the two particles aggregate to form an aggregate. If the turbulence shear stress is larger than the adhesive force of the aggregate, it will breakup, as shown at time of about 4.8 s. At 6.3 s, particle 36 and 86 collide and aggregate again.

The following describes the formation of a three-particle aggregate at shear rate $G=17.6$ s^{-1} (Fig. 12), the distance between particle 36 and particle 86 is close at time of about 5 s to show a sharp increase of forces between them. As the
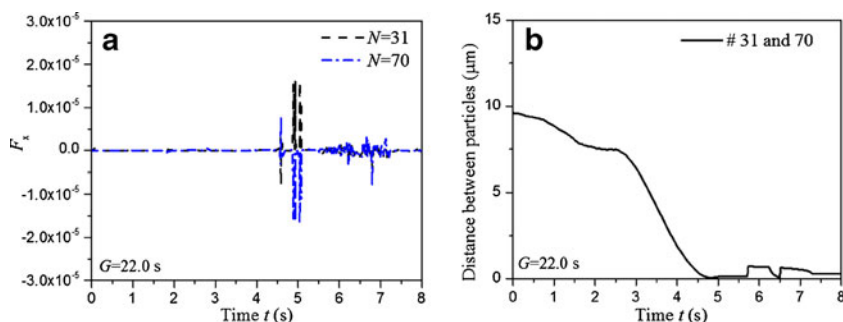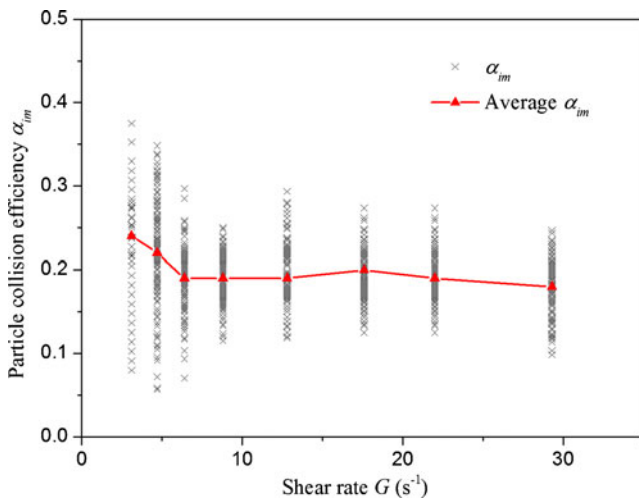
Fig. 14 Particle collision efficiency of the aggregates in the different turbulent shear rates of 3.1, 4.7, 6.4, 8.8, 12.8, 17.6, 22.0, 29.3 s^{-1}

Fig. 15 Relationship between the collision frequency and the shear rate. *Solid square* means numerical results at 180 s and *hollow square* stands for the theoretical results

distance between them is about $0.01d_p$, a two particle aggregate is formed. At $t=5.5$ s, the aggregate catches another particle, particle 30 to form a new aggregate when the distance between the particle 36 and 30 reduces to $0.01d_p$. Higher shear rate may provide better opportunities to form a three-particle aggregate.

The higher shear rate may also increase the opportunity of aggregate breakage in turbulent flow. An example with $G=22.0$ s^{-1} (Fig. 13) shows the collision of particles 31 and 70 and forms a new aggregate at $t\approx5$ s. The higher shear rate value breaks the aggregate at $t=5.7$ s, when the distance between particles becomes bigger than $0.01d_p$. Then, the processes of the floc breakage and re-flocculation take place by turn.

The particle collision efficiency of the aggregates in different shear turbulent conditions are obtained based on the analysis of interaction forces between particles (Fig. 14). If we track a particle, the particle collides with other particles when the forces on the particles increase sharply. As the distance between them is less than $0.01d_p$, the particle catches the other particle to form a floc. So, the likelihood for two particles to adhere and glue together after collision, i.e., the collision efficiency α_{im}, will be achieved. The average collision efficiency factor α_{im} can be calculated as 0.24, 0.22, 0.19, 0.19, 0.19, 0.20, 0.19, and 0.18 for the eight shear rates, respectively. Although higher shear rates will increase the particle collision frequency due to the higher turbulent kinetic energy, particle collision efficiency will decrease with G (Fig. 14). As Li and Logan (1997) discussed, the potential due to the increasing particle collision frequency by higher velocity will be partially offset by less contact time between the particles. As a result, the particle collision efficiency decreases with the shear rates.

4.5 Particle collision frequency function

The number of collisions between two particles with size i and size m per unit time per unit volume can be expressed by
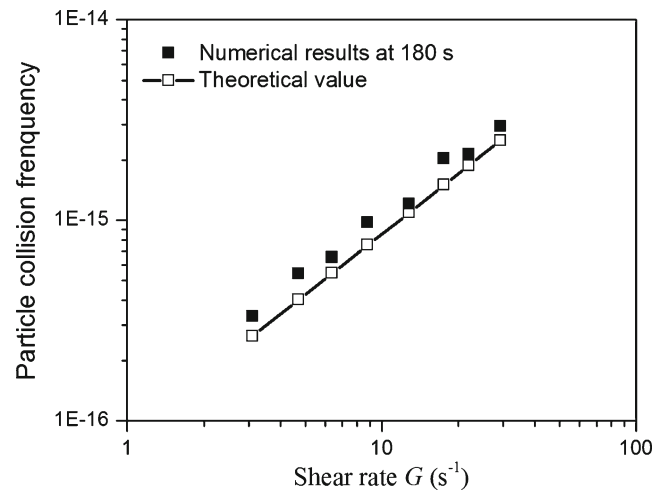
$N_{im}=\alpha_{im}\beta_{im}n_in_m$ (Smoluchowski 1917), in which, n_i and n_m are the number concentration of sizes i and m particles, respectively, β_{im} is a collision frequency function. In the LB simulation, the number of collisions between two particles N_{im}, n_i, n_m, and α_{im} can all be acquired from the numerical model results directly. Thus, the collision frequency function β_{im} can be estimated at any time. Here, the estimated β_{im}, at $t=180$ s, is plotted as the solid square in Fig. 15.

If shear is the only parameter that controls the flocculation mechanism, a collision frequency function β_{im} can be expressed by $\beta_{im}=G (d_i+d_m)^3/6$, in which d_i and d_m are diameters of the i and m particles, respectively (McCave 1984). If d_i and d_m are selected as 3 and 5 μm (the minimum and maximum primary particle size in the model), respectively, the collision frequency β_{im} may be obtained (open squares in Fig. 15). But d_i and d_m are not limited to only 3 and 5 μm.

Compared with the numerical results and the theoretical values, it can be seen that the calculations by LB model is slightly larger than that obtained by theoretical equation. It is because that the empirical equation only considers the shear rate, but the coagulations due to differential settling are also included in the numerical model. Nevertheless, Fig. 15 shows that flow shear rate contributes much more in flocculation than differential settling. It could be concluded that the role of differential settling on flocculation processes may be ignored for shear rates in the simulation range of 3.1–29.3 s^{-1}. Moreover, it also concluded that the collision frequency can be calculated directly using the simple empirical equations.

5 Conclusions

A numerical model on micro-scale simulation of turbulence-induced flocculation processes of fine sediments was established via LB method to explore aggregation mechanisms,

to examine the development of flocs at early-stage and steady-state flocculation. Although this model uses perfect spherical particles as the primary particles, only one salinity environment, and only one initial concentration, 2.0 kg m^{-3}, for the suspended sediment with a narrow band on primary particle size (3 to 5 μm), it is the first step toward the simulation of true cohesive sediment flocculation.

The flocculation and settling of selected sediment with different turbulent shear rates, $G = 3.1$, 4.7, 6.4, 8.8, 12.8, 17.6, 22.0, and 29.3 s^{-1}, were simulated, respectively. The time evolution of floc size, floc size distribution, and floc settling velocity were examined through the numerical model. The dimensionless floc size $d_f/d_{f,ave}$ distributions present a time-independent pattern during early-stage flocculation. During steady-state flocculation, from the floc size distributions, it can be seen that increasing shear rate reduces the large tail of distribution and decreases the range of floc size distributions. However, the shear rate has no effect on the shape of normalized steady-state floc size distribution.

The floc size, settling velocity and effective density at the non-equilibrium flocculation do not change obviously for shear stresses in the range 0–0.4 N m^{-2}. Comparison of the relation between floc size and settling velocity established during floc growth with the corresponding steady-state relation reveals that the different relations lead to the mean fractal dimension decreasing at the end of the growth period.

Additionally, hydrodynamic forces on the sediment particles were obtained directly from the numerical model. Low shear rate would encourage the floc formation. The opposite trend is observed at high shear rate. So it can be seen that the turbulence-induced flocculation was a combined process of aggregation and floc breakup based on the forces acting on sediment particles. Furthermore, the collision frequency and aggregate efficiency can be obtained directly through simple statistics of numerical results via LB model, which is attributed to precise description of each sediment particle and inter-particle forces in LB model. From this modeling exercise, it can be concluded that turbulent shear has a significant influent factor on the floc size, floc settling velocity, and collision frequency.

It is understood that non-spherical particles should be used in the modeling of collision, aggregation, breakup, and settling. Furthermore, clay mineral and organic matter, consists mainly of polymers (Manning et al. 2007), is another major factor responsible for mud flocculation. Biological coating of the particles will also affect the particle characteristics (Amos et al. 2010). As a perspective, the model may include some parameters to simulate non-spherical particles, polymers, and some biological coating effects.

References

Amos CL, Droppo IG (1996) The stability of remediated lake bed sediment, Hamihon Harbour, Lake Ontario, Canada. Geological Survey of Canada Open File Report. 2276

Amos CL, Umgiesser G, Ferrarin C, Thompson CEL, Whitehouse RJS, Sutherland TF, Bergamasco A (2010) The erosion rates of cohesive sediments in Venice lagoon, Italy. Cont Shelf Res 30:859–870

Camp TR, Stein PG (1943) Velocity gradients and internal work in fluid motion. J Boston Soc Eng 30:219–237

Cate AT, Derksen JJ, Portela LM (2004) Fully resolved simulations of colliding monodisperse spheres in forced isotropic turbulence. J Fluid Mech 519:233–271

Chen H, Chen S, Matthaeus WH (1992) Recovery of the Navier–Stokes equations using a lattice-gas Boltzmann method. Phys Rev A 45: R5339–R5342

Chen S, Doolen GD (1998) Lattice Boltzmann method for fluid flows. Annu Rev Fluid Mech 30:329–364

Frappier G, Lartiges BS, Skali-Lami S (2010) Floc cohesive force in reversible aggregation: a Couette laminar flow investigation. Langmuir 26(13):10475–10488

Ha HK, Maa JPY (2010) Effects of suspended sediment concentration and turbulence on settling velocity of cohesive sediment. Geosci J 14(2):163–171

Hamaker HC (1937) The London–van der Waals attraction between spherical particles. Physica 4(10):1058–1072

Hiemenz PC (1986) Principles of colloid and surface chemistry. New York

Higashitani K, Iimura K (1999) Two-dimensional simulation of the breakup process of aggregation in shear and elongational flows. J Colloid Interface Sci 204:320–327

Higashitani K, Iimura K, Sanda H (2001) Simulation of deformation and breakup of large aggregates in flows of viscous fluids. Chem Eng Sci 56:2927–2938

Hill RJ, Koch DL, Ladd AJC (2001) The first effects of fluid inertia on flows in ordered and random arrays of spheres. J Fluid Mech 448:213–241

Huang H (1994) Fractal properties of flocs formed by fluid shear and different settling. Phys Fluids 36(10):3229–3234

Hunt JR (1982) Self-similar particle-size distributions during coagulation: theory and experimental verification. J Fluid Mech 122:169–185

Kim S, Karrila SJ (1991) Microhydrodynamics: principles and selected applications. Butterworth-Heinemann, Boston

Ladd AJC (1994) Numerical simulations of particulate suspensions via a discretized Boltzmann equation. Part 1. Theoretical foundation. J Fluid Mech 271:285–309

Ladd AJC, Verberg R (2001) Lattice-Boltzmann simulations of particle-fluid suspensions. J Stat Phys 104:1191–1251

Lee DG, Bonner JS, Garton LS, Ernest ANS, Autenrieth RL (2000) Modeling coagulation kinetics incorporating fractal theories: a fractal rectilinear approach. Water Res 34(7):1987–2000

Li XY, Logan BE (1997) Collision frequencies between fractal aggregates and small particles in turbulently sheared fluid. Environ Sci Technol 31:1237–1242

Liebovitch LS, Toth T (1989) A fast algorithm to determine fractal dimensions by box counting. Phys Lett A 141(8–9):386–390

Liu QZ, Li JF, Dai ZJ, Li DJ (2007) Flocculation process of fine-grained sediments by the combined effect of salinity and humus in the Changjiang Estuary. Acta Oceanol Sin 26(1):140–149

Lundgren TS (2003) Linearly forced isotropic turbulence. Annual Research Briefs. 461–473

Machiels L (1997) Predictability of small-scale motion in isotropic fluid turbulence. Phys Rev Lett 79(18):3411–3414

Maggi F (2005) Flocculation dynamics of cohesive sediments. Dissertation, Delft University of Technology

Maggi F, Mietta F, Winterwerp JC (2007) Effect of variable fractal dimension on the floc size distribution of suspended cohesive sediment. J Hydrol 343(1–2):43–55

Manning AJ (2004) The observed effects of turbulence on estuarine flocculation. J Coast Res 41:90–104, SI

Manning AJ, Dyer KR (1999) A laboratory examination of floc characteristics with regard to turbulent shearing. Mar Geol 160:147–170

Manning AJ, Friend PL, Prowse N, Amos CL (2007) Estuarine mud flocculation properties determined using an annular mini-flume and the LabSFLOC system. Cont Shelf Res 27:1080–1095

McCave IN (1984) Size spectra and aggregation of suspended particles in the deep ocean. Deep-Sea Res 31(4):329–352

Mietta F, Chassagne C, Manning AJ, Winterwerp JC (2009) Influence of shear rate, organic matter content, pH and salinity on mud flocculation. Ocean Dyn 59:751–763

Nguyen NQ, Ladd AJC (2002) Lubrication correction for lattice-Boltzmann simulations of particle-fluid suspensions. Phys Rev. E66: 046708-1–11

Russel WB, Saville DA, Schowalter WR (1989) Colloidal dispersions. Cambridge University Press, Cambridge

Smoluchowski M (1917) Versuch einer mathematischen theorie der koagulations-kinetik kolloider losunge. Z Phys Chem 92:129–168

Spicer PT, Pratsinis SE (1996) Shear-induced flocculation: the evolution of floc structure and the shape of the size distribution at steady state. Water Res 30(5):1049–1056

Tang S, Ma Y, Shiu C (2001) Modeling the mechanical strength of fractal aggregates. Colloids Surf A Physicochem Eng Asp 180(1):7–l6

Verway EJ, Overbeek JTG (1948) Theory of the stability of hyophobic colloids. Elsevier, Amsterdam

Winterwerp JC (1998) A simple model for turbulence induced flocculation of cohesive sediment. J Hydraul Res 36(3): 309–326, IAHR

Winterwerp JC, Manning AJ, Martens C, de Mulder T, Vanlede J (2006) A heuristic formula for turbulence-induced flocculation of cohesive sediment. Estuarine Coastal Shelf Sci 68:195–207

Xu FH, Wang DP, Riemer N (2008) Modeling flocculation processes of fine-grained particles using a size- resolved method: comparison with published laboratory experiments. Cont Shelf Res 28:2668–2677

Yan P, Wei L, Luo LS, Wang LP (2010) Comparison of the lattice Boltzmann and pseudo-spectral methods for decaying turbulence: low-order statistics. Comput Fluids 39:568–591

Zeidan M, Xu B, Jia X (2007) Simulation of aggregate deformation and breakup in simple shear flows using a combined continuum and discrete model. Chem Eng Res Des 85(12):1645–1654

Zhang JF, Zhang QH (2009) Hydrodynamics of fractal flocs during settling. J Hydrodyn 21(3):347–351

Zhang JF, Zhang QH (2011) Lattice Boltzmann simulation of the flocculation process of cohesive sediment due to differential settling. Cont Shelf Res 31:S94–S105

Zhang QH, Zhang JF (2007) Modeling of 3D fractal mud flocs settling via lattice Boltzmann method. In: Sediment and Ecohydraulics - Proc. in Marine Science, INTERCOH 2005. Elsevier, Amsterdam